ALGORITHM THEORETICAL BASIS DOCUMENT

RAMSES II

Retrieval Algorithm for Microwave Sounders in Earth Science

The NASA ATMS Retrieval System

Level 2

Bjorn Lambrigtsen
Evan Fishbein
Mathias Schreier

Jet Propulsion Laboratory
California Institute of Technology

Version 1 June 2021

The research was carried out at the Jet Propulsion Laboratory, California Institute of Technology, under a contract with the National Aeronautics and Space Administration (80NM0018D0004).

Relevant Documents

AIRS L2 ATBD, JPL D-17006, Version 4.0, 1 March 2007
ATMS L1b ATBD, Version 1, July 2014

Acknowledgment

The initial implementation of the ATMS L2 algorithm – the baseline – is nearly identical to the AMSU/HSB algorithm developed by P. Rosenkranz for AIRS, and this ATBD reflects that heritage.

Version History

V0	Initial draft	July 2017
V1a	Version delivered to Sounder SIPS	December 2020
V1	Renamed for RAMSES II release	June 2021

1. Introduction

This Level 2 ATBD describes the theoretical basis and, to some extent, the implementation of the algorithms used to convert brightness temperatures (Tb) to geophysical quantities (temperature and water vapor profiles, etc.) for ATMS. The algorithms described here are essentially the same as the Aqua AMSU/HSB "microwave-only" algorithms, which is the baseline for this development. Further development is planned to implement improvements.

It is the intention that this ATBD be readable as a standalone document, and some material is therefore included from the ATMS L1b ATBD. In what follows there is a brief description of the instrument itself, in order to explain references to devices, procedures and tables used by the L1b algorithms.

This document describes the functions performed by the retrieval system. However, it should be noted that nothing should be implied about the architecture or the software implementation of the system. Thus, algorithms that may be described here as if they were to be executed in conjunction with each other could in fact be executed in isolation from each other. For example, data quality checking belonging to individual steps may be consolidated and executed before those steps are reached in the actual processing system, in order to provide an efficient implementation. Also, in some instances there may be essential elements missing from the software implementation – those will be noted in the text and in a companion commentary.

We note in particular that the retrieval algorithms operate on brightness temperatures (Tb) and not antenna temperatures (Ta). It is necessary to account for scan bias and other antenna effects to convert from Ta to Tb. This may be done as an L1 post-processing step or an L2 pre-processing step. This ATBD does not address that step.

2. Historical Perspective

The Advanced Technology Microwave Sounder (ATMS), together with the Crosstrack Infrared Sounder (CrIS) — a high spectral resolution IR spectrometer — are designed to meet the measurement requirements set for the National Polar-orbiting Operational Environmental Satellite System (NPOESS), now succeeded by the Joint Polar Satellite System (JPSS), as well as satisfy the climate research needs of the National Aeronautics and Space Administration (NASA). The first version of this Crosstrack Infrared Microwave Sounding Suite (CrIMSS) was initially operated by NASA on the National Polar Partnership mission (NPP), previously called the NPOESS Preparatory Project, and later handed over to JPSS as an operational mission. NPP serves the two functions of providing risk reduction for JPSS and providing science data continuity between the NASA Terra and Aqua missions (the latter being the first mission to carry a high resolution sounding suite) on one hand and JPSS on the other. For that reason, the NPP mission has sometimes been called the “bridging mission”. Additionally, while JPSS is primarily designed to support operational weather forecasting needs, NASA has a strong interest in research and climate applications, and an effort is under way to determine how JPSS can satisfy those needs as well. Thus, the third function of NPP is to serve as a testbed for transforming weather satellite data to climate research quality data.

The High Resolution Infrared Sounder (HIRS) and the Microwave Sounding Unit (MSU), together forming the TIROS Operational Vertical Sounder (TOVS) on the NOAA polar orbiting environmental satellite system (POES), have supported the National Weather Service (NWS) forecasting effort with global temperature and moisture soundings since the late 70's. In the course of the years HIRS has been periodically upgraded, and in 1998 a jump was made from MSU to the Advanced Microwave Sounding Unit (AMSU). The combined HIRS/AMSU system is called the Advanced TOVS (ATOVS) and has formed the backbone of the NOAA POES systems and is also implemented on the Eumetsat Metop systems. It is expected to operate well into the first JPSS mission proper (JPSS-1).

During the mid-1980’s, while TOVS was still flying, it was determined that future numerical weather prediction (NWP) data needs would soon require satellite sounders with accuracies equivalent to radiosondes. An effort was launched by NASA to develop the technology and capability to achieve that. The result was the Atmospheric Infrared Sounder (AIRS), which, together with an AMSU microwave suite, was launched as part of the Aqua mission in 2002. AIRS was the first of a series of high spectral resolution IR sounders, and it has already demonstrated the utility of radiosonde quality satellite soundings – AIRS data is now being assimilated by a number of NWP centers and is having significant positive forecast impact. CrIS uses a different measurement approach (it is a Fourier transform spectrometer, while AIRS is a grating spectrometer), but it is the successor of AIRS and is expected to have comparable performance. Other instruments in the same class are being developed elsewhere.

During the mid-1990’s, while AIRS was being built, an effort was made by NASA to transfer the AIRS technology to the Integrated Program Office (IPO), which was managing the NPOESS mission, with the goal of providing an AIRS follow-on for the NPOESS

missions. Again, a technology development effort was launched – this time primarily focused on reducing the mass, size and power consumption of the microwave component of the sounding suite. The proposed system – the Integrated Multispectral Atmospheric Sounder (IMAS) – was a single combined infrared and microwave instrument that was intended to fly as a demonstration on the NASA New Millennium Program's EO-3 mission. The effort was terminated in mid-1998 largely due to cost constraints, but many of the IMAS microwave specifications were later adopted for the ATMS instrument.

It was initially the intention to use the 118-GHz oxygen line for temperature sounding in the IMAS system, instead of the 50-60 GHz band used by AMSU. This would make it possible to shrink the aperture by a factor of more than 2 (and therefore also the overall mass and size) while maintaining spatial resolution and other performance measures. A field of view (FOV) of the same size as the IR sounder (i.e. 1.1°) was highly desired, and the IMAS/MW component was therefore designed to have that beam width for all sounding channels (i.e. in the 118-GHz band for temperature sounding and in the 183-GHz band for water vapor sounding). Later, it was realized that even the most transparent 118-GHz channels may not be able to penetrate to the surface under very humid and cloudy conditions (e.g., in the tropics), and the 50-GHz band was restored to provide backup capabilities for such situations. A compromise was made to use the same aperture size at 50 GHz as at 118 GHz, and a 2.5° beam width resulted. The IMAS team also determined that the microwave instrument should have the same spectral channels as AMSU for "science continuity" and that a few additional channels were desirable. Thus, two channels were added in the 183-GHz band, and one window channel was added in the 50-GHz band. In addition, the 150-GHz quasi-window channel used in AMSU-B was replaced with one at 166 GHz, which can be operated as part of an advanced-technology 183-GHz receiver (thus saving one receiver chain). This concept had been developed earlier by the AIRS team. Most of these specifications and characteristics are now part of the ATMS specifications, but the 118-GHz band was eliminated early in the program due to cost constraints, and 2.5° was changed to 2.2°.

The most significant advance under IMAS was the development of monolithic microwave integrated circuit (MMIC) technology at sounding frequencies (i.e. at 50, 118 and 183 GHz) – previously only available at considerably lower frequencies, which would allow for sensitive and compact receivers and spectrometers. Sample receivers were developed for the two lower bands, and low noise amplifiers (i.e. precursors to full receivers) were developed for the 183-GHz band, and compact solid-state filter banks were developed for the two lower bands. After the termination of IMAS these technology items were incorporated into an aircraft based microwave sounder, the High Altitude MMIC Sounding Radiometer (HAMSR), developed under the NASA Instrument Incubator Program. HAMSR may be viewed as an ATMS precursor and prototype in many respects (e.g., HAMSR uses a dual aperture, with two reflectors operating on a common axis, just as was later adopted for ATMS). HAMSR has been successfully operated on NASA high altitude aircraft since 2001. In summary, ATMS has heritage primarily from AMSU and from the IMAS design (and its HAMSR spin-off).

3. Instrument Description

In this section we give a brief description of the ATMS instrument, illustrated in Fig. 1. ATMS is

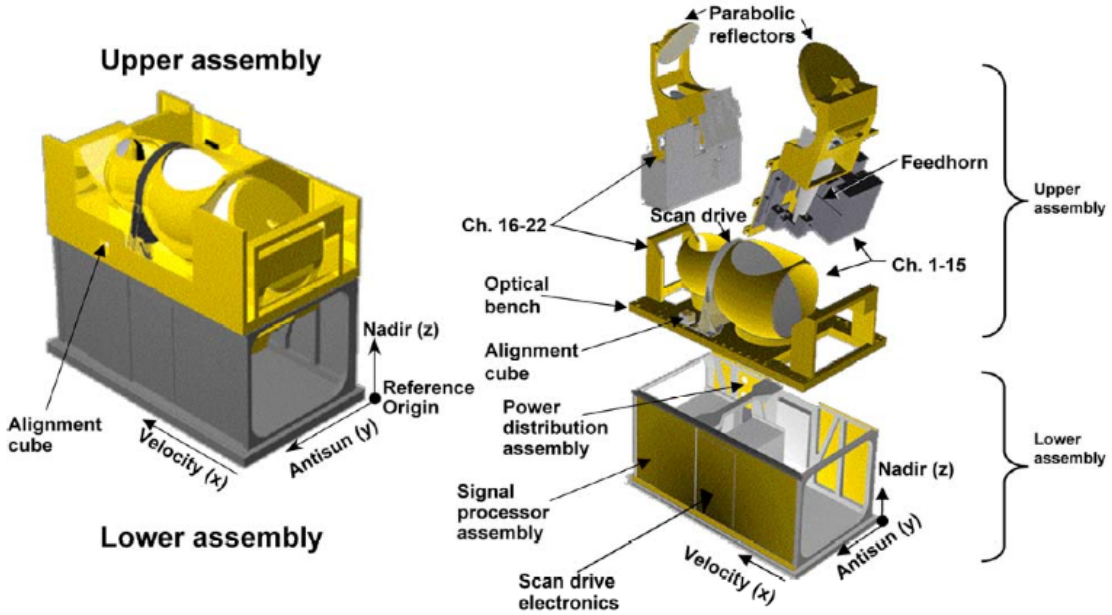

Figure 1: ATMS instrument layout

a 22-channel microwave sounder providing both temperature soundings – between the surface and the upper stratosphere (i.e. to about 1 mb, at an altitude of about 45 km) – and humidity soundings – between the surface and the upper troposphere (i.e. to about 200 mb, at an altitude of about 15 km). Like AMSU, it is a crosstrack scanner. There are two receiving antennas — one serving 15 channels below 60 GHz (with a beam width of 2.2° for all except the lowest two channels) and one serving 7 channels above 60 GHz (with a beam width of 1.1° for all except the lowest channel). The antennas consist of plane reflectors mounted on a scan axis at a 45° tilt angle, so that radiation is reflected from a direction perpendicular to the scan axis into a direction along the scan axis (i.e. a 90° reflection). With the scan axis oriented in the along-track direction, this results in a cross-track scan pattern. The reflected radiation is in each case focused by a stationary parabolic reflector onto a dichroic plate and from there either reflected to or passed through to a feedhorn. Each aperture/reflector therefore serves two frequency bands, for a total of four bands. Thus, radiation from a direction within the scan plane, which depends on the angle of rotation of the reflector, is reflected and focused onto the receiver apertures — conical feedhorns. This is illustrated schematically in Fig. 2.

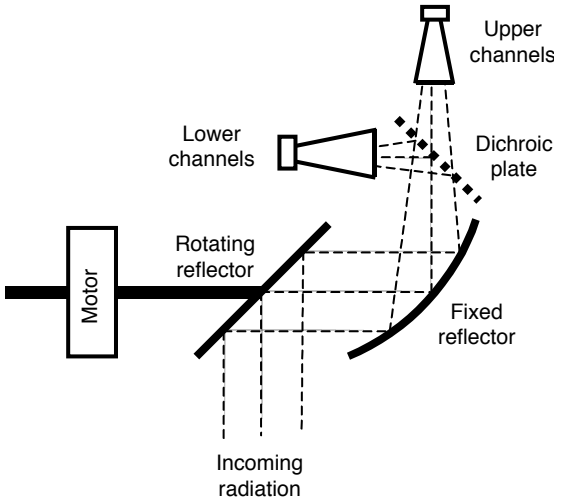

Figure 2: ATMS antenna and RF feed subsystem (schematically): one of two

The design of the antenna system is such that a slightly diverging conical pencil "beam" is

formed which has a half-power width (also called the 3-dB width) of either 1.1°, 2.2° or 5.2°, with a possible ±10% variation from channel to channel. Each beam is approximately Gaussian-shaped at the center and receives a significant portion of its energy outside the half-power cone. Approximately 95-97% of the energy is received within the so-called main beam, which is defined as 2.5 times the half-power beam width — i.e. the ATMS "main beam" is either 2.75°, 5.5° or 13° wide. Significant energy (i.e. up to 5%) is thus received from outside the main beam. Fig. 3 shows a typical antenna pattern. The pattern in the vicinity of the main beam is called the near sidelobes, while that further away is called the far sidelobes. The far sidelobes contribute significantly to the measurement errors.

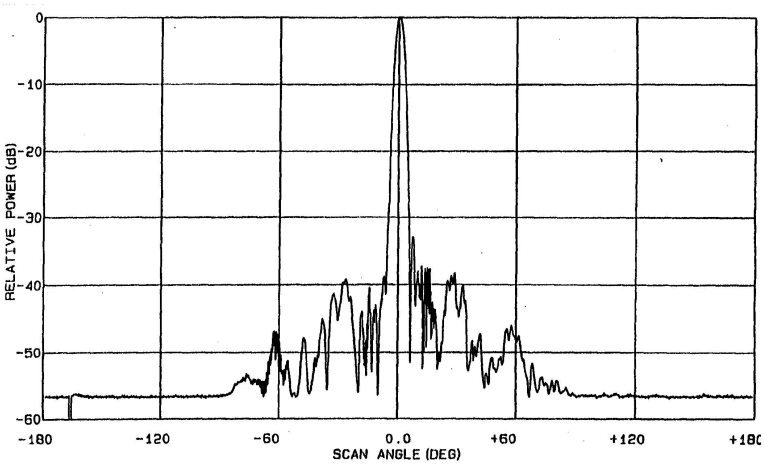

Figure 3: Typical microwave antenna pattern

The feedhorn is for some bands followed by a diplexer that splits the RF energy into two parallel signal paths that proceed to the respective receiver, which is in most cases a heterodyne system. There, each sub-band is down converted by a mixer, separated into channels with filters, and detected. Fig. 4 shows a block diagram of the ATMS system. In the following paragraphs we will

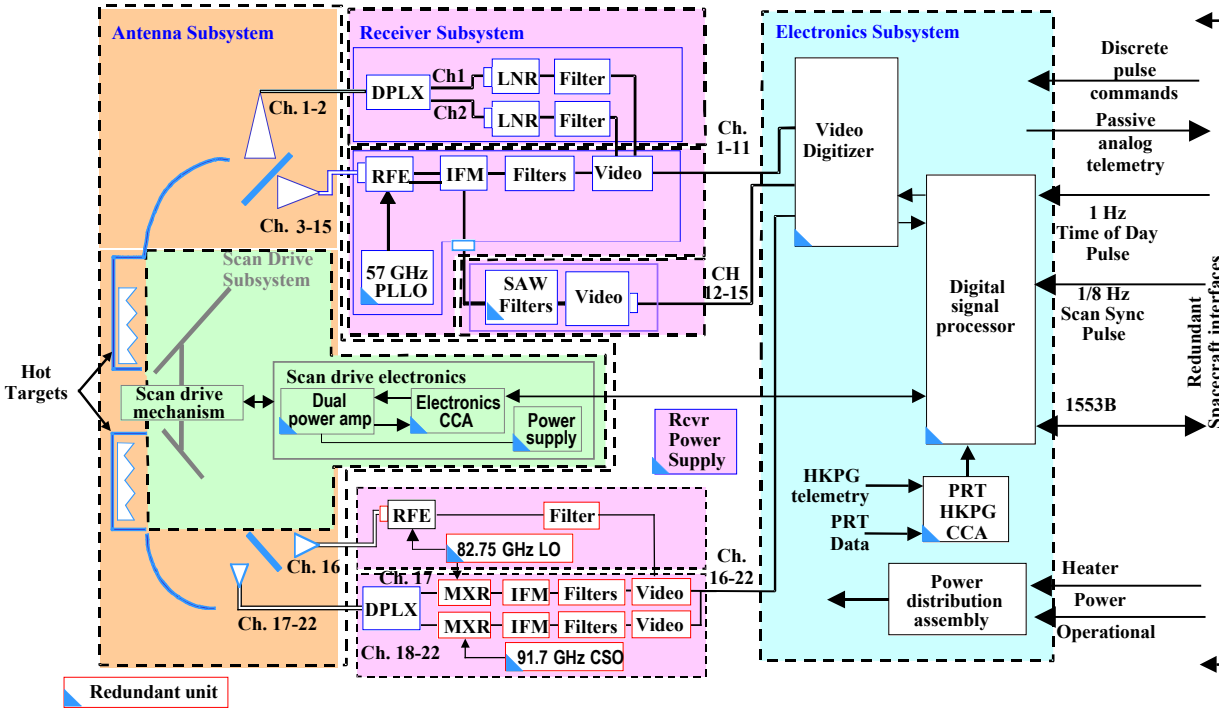

Figure 4. ATMS block diagram

discuss the various signal paths that lead to the individual spectral channel outputs.

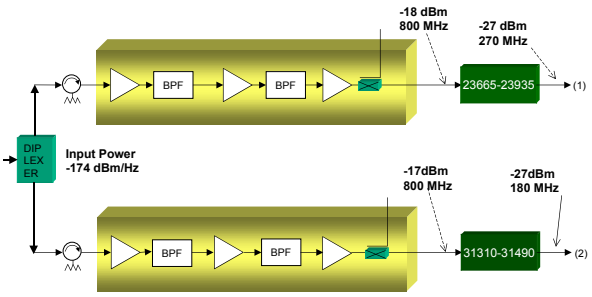

Figure 5. Lowest-frequency receivers

The larger of the two apertures is used for the 15 lowest-frequency channels and is some times referred to as the KAV-aperture, since it covers K-band (channel 1), Ka-band (channel 2) and V-band (channels 3-15). Here the dichroic plate, which reflects frequencies below a certain value and transmit those above, splits the RF energy into a low frequency path (reflected) and a high frequency path (transmitted). The output of the low frequency feedhorn enters a diplexer, which in turn splits the now somewhat band limited RF energy into two parallel paths. Each is fed into an amplified receiver chain followed by a bandpass filter – one centered at 23.8 GHz (channel 1) and one centered at 31.4 GHz (channel 2). These are the only non-heterodyne receivers in the ATMS system. Fig. 5 illustrates this subsystem.

The output of the higher frequency feedhorn is fed into an amplified and bandpass filtered heterodyne receiver with two down-converter/mixer chains, both fed by a common local oscillator (LO) operating at 57.290344 GHz. (This is a highly stable and temperature controlled crystal referenced phase locked oscillator.) One path is low pass filtered, and the result is a single-sideband intermediate frequency (IF) band located at 1.6 – 7.1 GHz below the LO frequency. This band is in turn passed through a set of signal splitters/multiplexers and bandpass filters that select channels 3-9. The other path is bandpass filtered, and the result is a double-sideband IF band located 10 – 400 MHz away from the LO frequency. Two channels (10 and 11) are formed with conventional bandpass filters similar to those used for channels 3-9, while the rest (12-15) are formed with a standing acoustic wave (SAW) filter assembly. This is illustrated in Fig. 6. Note that the SAW assembly is implemented as a set of four pairs of filters, each positioned symmetrically with respect to an IF frequency of 322.2 MHz. The outputs of each filter pair are combined and amplified.

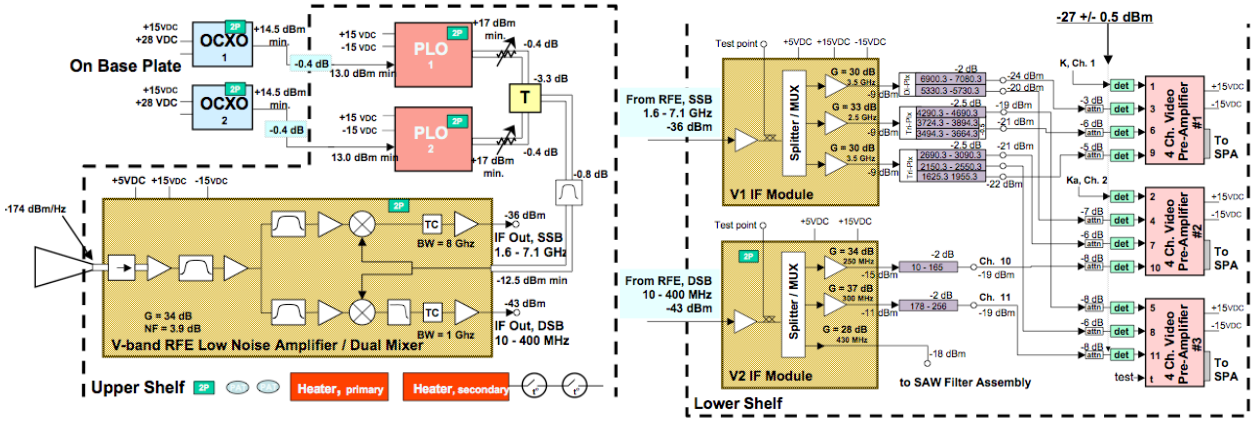

Figure 6. Channel 3-15 receiver subsystem

Channels 12-15 are therefore in effect quadruple-sideband channels.

The smaller aperture is used for the 7 highest frequency channels and is some times referred to as

the WG-aperture, since it covers W-band (channel 16) and G-band (channels 17-22). Here the lower frequency path (i.e. reflected from the dichroic plate) enters a single feedhorn and an amplified highpass filtered heterodyne receiver chain, where the mixer uses an LO operating at 82.75 GHz, producing a single upper sideband IF signal that is put through a 4450-6450 MHz bandpass filter for channel 16 (which results in a channel located at 87.2-89.2 GHz). The high frequency path (i.e. that transmitted through the dichroic plate) enters a smaller feedhorn followed by a diplexer that splits the signal into two paths. One path goes to a second harmonic mixer that uses the same LO as the channel 16 receiver. The resulting double sideband IF signal is put through a 350-1500 MHz bandpass filter for channel 17 (which is then located at 164-167 GHz with a gap at 165.15-165.85 GHz). The second path also goes to a second harmonic mixer, but it uses an LO operating at 91.655 GHz. The double sideband IF is passed through a set of filters that produce channels 18-22. (Those channels are therefore centered at 183.31 GHz ± Δf, where Δf is 7, 4.5, 3, 1.8 or 1 GHz, and the bandpass width varies from channel to channel.) This subsystem is illustrated in Fig. 7.

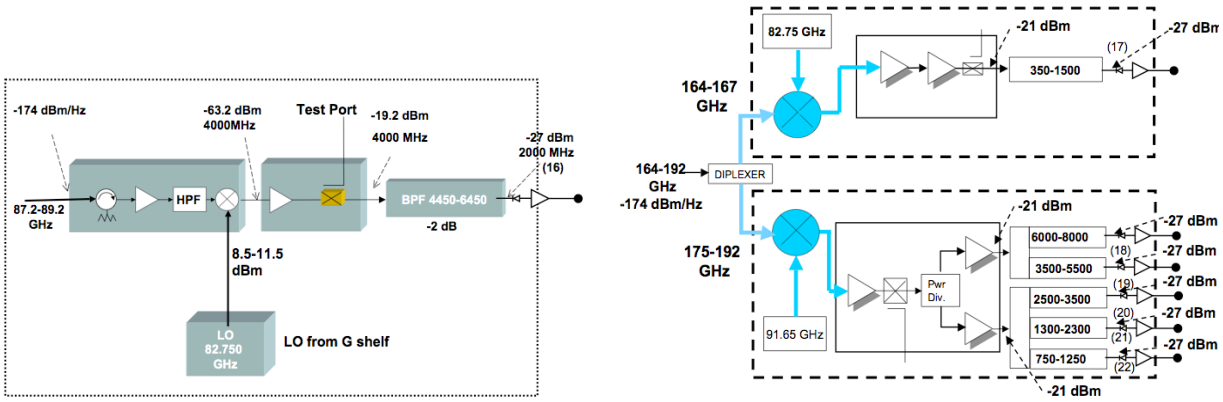

Figure 7. Channel 16 and 17-22 receiver subsystems

Table 1 summarizes the performance specifications of all 22 channels, including radiometric sensitivity – usually called noise equivalent temperature change and denoted as NEDT, which is listed in terms of specifications, measured performance on the ground and measured performance on-orbit. The table lists three frequency specifications: nominal center frequency, center frequency stability (i.e. the maximum deviation allowed from the nominal center frequency value), and specified and as-built bandwidth. All are given in MHz. The as-built bandwidth notation is "NxΔf", where N is the number of sub-bands used for a channel and Δf is the width of each sub-band. (E.g., 2x270 means this is a double-band channel, with each of the two bands being 270 MHz wide.)

Beamwidth and beam efficiency (computed from measured antenna patterns) are also listed. Finally, the polarization of each channel is listed. A single linear polarization is measured for each channel, and Table 1 lists the nominal polarization direction at the nadir scan position.

Table 1. ATMS spectrometric and radiometric specifications

Ch	RF path			Center frequency [MHz]		Bandwidth [MHz]		NEDT [K]			Pol	Beamwidth [°]	Beam eff.
	Ant	Feed	Rcvr	Value	Stab	Req	True	Req	T/V	Op'l		Req	[%]
1	A	1	a	23800	<10	<270	1x270	0.5	0.2	0.2	V	5.2	99.6
2	A	1	b	31400	<10	<180	1x180	0.6	0.3	0.3	V	5.2	99.6
3	A	2	c	50300	<10	<180	1x180	0.7	0.4	0.3	H	2.2	99.4
4	A	2	c	51760	< 5	<400	1x400	0.5	0.3	0.3	H	2.2	99.5
5	A	2	c	52800	< 5	<400	2x170	0.5	0.3	0.3	H	2.2	99.5
6	A	2	c	53596±115	< 5	170	1x170	0.5	0.3	0.3	H	2.2	99.4
7	A	2	c	54400	< 5	400	1x400	0.5	0.3	0.3	H	2.2	99.5
8	A	2	c	54940	<10	400	1x400	0.5	0.3	0.3	H	2.2	99.5
9	A	2	c	55500	<10	330	1x330	0.5	0.3	0.3	H	2.2	99.5
10	A	2	d_1	57290.344 [f_0]	<0.5	330	2x155	0.75	0.4	0.4	H	2.2	99.5
11	A	2	d_1	f_0±217	<0.5	78	2x 78	1.0	0.5	0.5	H	2.2	99.5
12	A	2	d_2	f_0±322.2±48	<1.2	36	4x 36	1.0	0.6	0.5	H	2.2	99.5
13	A	2	d_2	f_0±322.±22	<1.6	16	4x 16	1.5	0.8	0.8	H	2.2	99.5
14	A	2	d_2	f_0±322.±10	<0.5	8	4x 8	2.2	1.2	1.1	H	2.2	99.5
15	A	2	d_2	f_0±322.±4.5	<0.5	3	4x 3	3.6	1.8	1.8	H	2.2	99.5
16	B	3	e	88200	<200	2000	1x2000	0.3	0.3	0.3	V	2.2	97.7
17	B	4	f	165500	<200	3000	2x1150	0.6	0.4	0.4	H	1.1	97.8
18	B	4	g	183310±7000	<30	2000	2x2000	0.8	0.3	0.4	H	1.1	97.8
19	B	4	g	183310±4500	<30	2000	2x2000	0.8	0.4	0.4	H	1.1	97.9
20	B	4	g	183310±3000	<30	1000	2x1000	0.8	0.5	0.5	H	1.1	98.5
21	B	4	g	183310±1800	<30	1000	2x1000	0.8	0.5	0.5	H	1.1	98.5
22	B	4	g	183310±1000	<30	500	2x 500	0.9	0.7	0.7	H	1.1	98.5

Because of the rotating main reflector, the detected polarization vector rotates as the scan reflector rotates. (This can be understood by envisioning the detected polarization vector, which is fixed relative to the feedhorn, being projected onto the ground below – by simple geometric imaging.) The direction indicated in Table 1 as "V" corresponds to a direction that lies in the scan plane, while "H" is the direction that is perpendicular to the scan plane – i.e. in the horizontal plane. (At nadir these two polarizations are degenerate, i.e. observed emissions would be identical for an isotropic surface.) As the scanner rotates the beam away from nadir, the detected "V" polarization also rotates out of the scan plane while the detected "H" polarization rotates out of the perpendicular plane and thus also out of the horizontal plane. The angle of rotation away from the respective planes equals the scan angle relative to nadir. This is illustrated schematically in Figure 8, which shows the projection of the various polarization vectors in the plane perpendicular to the ray path (i.e. the plane that contains the electromagnetic field vectors). This plane coincides with the horizontal plane for the nadir scan position but rotates as the scan position rotates. In addition, as explained above, the "H" and "V" polarization vectors rotate within this plane. When surface emissivity and similar quantities are computed, it is important to correctly transform between the observed "H" and "V" vectors and the local true H and V vectors as computed from models.

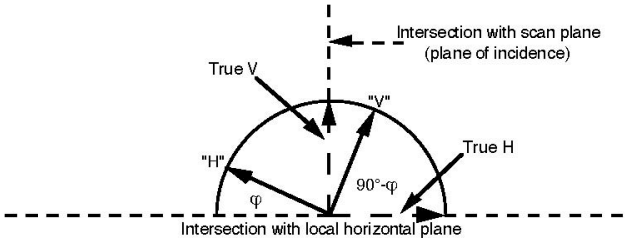

Figure 8. Polarization vectors, in the transverse plane

The antenna reflectors rotate continuously counter-clockwise relative to the spacecraft direction of motion (i.e. the spin vector points in the negative x-direction while the spacecraft moves along the positive x-direction), completing three revolutions in 8 seconds. The scan mechanism is synchronized to the spacecraft clock with a "sync" pulse every 8 seconds (i.e. for every third revolution). Each scan cycle is divided into three segments. In the first segment the earth is viewed at 96 different angles, symmetric around the nadir direction. The antenna is in continuous motion, and the 96 samples are taken "on the fly", with each sample representing the mid-point of a brief sampling interval of about 18 ms. The scan speed is such that the corresponding angular sampling interval is 1.11° (i.e. the scan speed is about 61.6°/second). The angular range between the first and last sample centroids is therefore 105.45° (i.e. ±52.725° relative to nadir). The antenna then accelerates and moves to a position that points it toward an unobstructed view of space (i.e. between the earth's limb and the spacecraft horizon). There it resumes the same slow scan speed as maintained across the Earth scenes while four consecutive cold calibration measurements are taken. Next, the antenna is again accelerated to the zenith direction, which points it toward an internal calibration target that is at the relatively high ambient instrument temperature, and is again slowed down to normal scan speed while four consecutive warm calibration measurements are taken. Finally, it is accelerated to the starting Earth scene position, where it is slowed down to normal scan speed to begin another scan cycle. Every third cycle the synchronization signal arrives just before the start position is reached and is used to maintain this pattern through a phase locked loop. Fig. 9 illustrates this — the normal operational scan mode. (There is also a stare mode, where the antenna can be pointed to the nadir direction or either of the calibration directions for an extended period of time, but that is only used for special purposes.) Each of the 96 earth samples takes about 18 milliseconds, for a total of approximately 1.73 seconds. The "duty cycle" of ATMS is therefore about 65%, i.e. about 65% of the scan cycle period is dedicated to Earth observations.

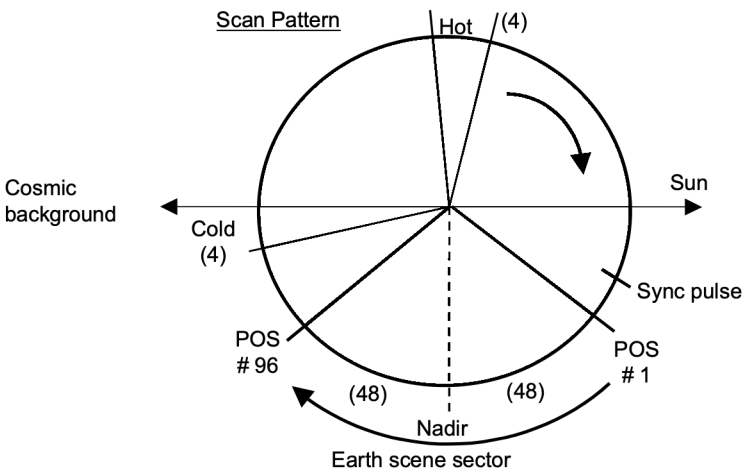

Figure 9. Scan sequence (flight direction is toward the reader)

As a result of unexpected wear on the scan mechanism, a new scan pattern was introduced on 8/24/2015, where the scanner is periodically reversed. That results in lubricant being redistributed, with consequent reduction in friction and an expected extension of system life time. The frequency of reversal was initially once a day, and it has since been increased to once per orbit. This is not expected to affect L2 processing, except that read software must be "aware" of the scan sequence.

4. The Forward Model

In the following, atmospheric radiative transfer or the 'forward problem' will be discussed. The physical retrieval methodology depends on the ability to accurately and rapidly calculate the outgoing radiance (brightness temperatures) based on the state of the surface and the atmosphere. Almost invariably, the statistical evaluation of calculated brightness temperatures, relative to those observed when the state of the atmosphere is reliably known, differs in the mean by a small, but significant amount, referred to as "bias." This bias may itself be a function of other parameters, such as the scan angle. The application of this bias in the retrieval process is described in Section 5.

At the frequencies measured by ATMS, the most important absorbing gases in the atmosphere are oxygen and water vapor. The oxygen molecule has only a magnetic dipole moment, and its lines are intrinsically much weaker than those which result from the electric dipole of water vapor; however, the much greater abundance of oxygen in the atmosphere more than compensates for this difference. When clouds are present, liquid water also plays a role in radiative transfer. However, fair-weather cirrus composed of ice particles small compared to the wavelength are generally transparent at ATMS frequencies.

1. Oxygen

O_2 spin-rotation transitions comprise approximately 30 lines between 50 and 70 GHz and an isolated line at 118.75 GHz (which is not observed by ATMS). Several groups have measured the pressure-broadened widths of the lines in the 50-70 GHz band. The line parameters used for the forward model are from the Millimeter-wave Propagation Model (MPM92) (Liebe, *et al.,* 1992). The characteristic of oxygen's microwave spectrum that introduces difficulty for construction of models is the significant degree of line mixing. In MPM92, line mixing was treated by a first-order expansion in pressure. The coefficients for this expansion were determined by a constrained linear fit to laboratory measurements made on an O_2 - N_2 mixture over the frequency range of 49-67 GHz and the temperature range 279-327 K, with a noise level of approximately 0.06 dB/km. Within that range, the model represents the measurements to $\leq$ 0.2 dB/km (see for example, Figure 10). It is possible that extrapolation to colder temperatures introduces larger errors. Measurements from the NASA ER-2 at 52-56 GHz (Schwartz, 1997) seem to be in agreement with the model, however.

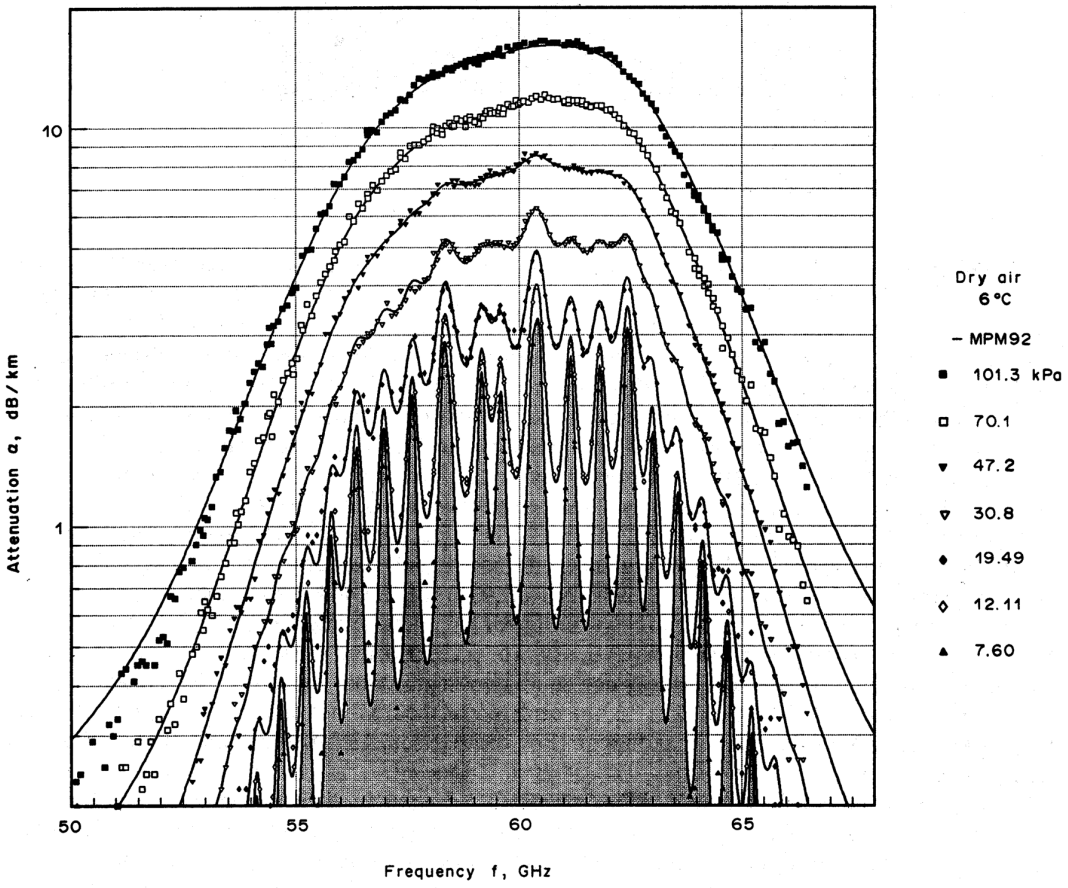

Figure 10. Millimeter-wave Propagation Model Example

2. Water Vapor

Water has a weak rotational line at 22.23 GHz that is semi-transparent at normal atmospheric humidity, and a much stronger, opaque line at 183.31 GHz. Intensities of these lines have been calculated and tabulated by Poynter and Pickett (1996 version of JPL line catalog) and Rothman, *et al*., (1998) (HITRAN), among others. The HITRAN intensities are used here. For the 22-GHz line, the JPL intensity is higher than the HITRAN value by 0.3%. There is a measurement by Liebe, *et al*., (1969) (estimated error 0.3%) which is 3.5% lower than the HITRAN value. At 183 GHz, the JPL line intensity is 0.1% higher than HITRAN. Widths have been measured by Liebe, *et al*., (1969) and Liebe and Dillon (1969) at 22 GHz with estimated uncertainty of 1% for both self and foreign-gas broadening; and by Bauer, *et al*., (1989) and Tretyakov, *et al*. (2003) at 183 GHz, with uncertainties of 0.5% for self-broadening and 1.0% for foreign-gas broadening, respectively. However, Gamache, *et al*., (1994) concluded from a survey of measurements of many H_2O lines that, in general, measured line widths should be considered to have uncertainties of 10-15%. The line at 183 GHz is a case in which published measurements of width differ significantly, but the value of Tretyakov, *et al*., (2003), which is used here, lies near the centroid of the measurements.

At frequencies away from these two lines, microwave absorption by water vapor is predominantly from the continuum, which is attributed to the low-frequency wing of the intense infrared and submillimeter rotational band lines. In the microwave part of the spectrum, the foreign-broadened component of the continuum is stronger than the self-broadened component, for atmospheric mixing ratios. Measurements of continuum absorption as a function of temperature have been made at various frequencies by Liebe and Layton (1987), Godon, *et al*. (1992) and Bauer, *et al*. (1993, 1995). There are also numerous measurements at single temperatures and frequencies in the laboratory, and in the atmosphere where temperature and mixing ratio are variable. The measurements do not present an entirely consistent picture. Rosenkranz (1998) proposed that the most satisfactory overall agreement with laboratory and atmospheric measurements of the water continuum was obtained with a combination of the foreign-broadened component from MPM87 (Liebe and Layton, 1987) with the self-broadened component from MPM93 (Liebe, *et al*., 1993). The combined model is used here.

3. Liquid Water

It is useful to distinguish between precipitating and non-precipitating clouds with respect to their interactions with microwaves. Over the range of wavelengths measured by ATMS, non-precipitating droplets (with diameters of 50 μm or less) can be treated using the Rayleigh small-droplet approximation. In this regime, absorption is proportional to the liquid water content of the air, and scattering can be neglected. The model for the dielectric constant limits the accuracy of these calculations. The double-Debye model of Liebe, *et al*., (1991) is used here; for temperatures > 0 °C, it has an estimated maximum prediction error of 3% between 5 and 100 GHz, and 10% up to 1 THz. Although some measurements of static dielectric constant at temperatures as low as –20 C were used by Liebe, *et al*. to develop their model, its use for supercooled water must be considered to be an extrapolation, with uncertain accuracy. (The model is implemented using the alternate eq. 2b in Liebe, *et al*.)

Precipitation, on the other hand, requires Mie theory to calculate both absorption and scattering. The latter is generally not negligible, and is the dominant term at some wavelengths. In the case of convective storms, scattering from ice at high altitudes is often the most important process. The rapid transmittance algorithm uses only the small-droplet approximation for cloud liquid water, and scattering is not included. For this reason, retrieved profiles with more than 0.5 kg/m^2 cloud liquid water are rejected, as probably rain-contaminated.

4. Rapid Transmittance Algorithm

The physical retrieval algorithm used for ATMS does radiative transfer calculations for each profile and hence needs a computationally efficient transmittance algorithm. The microwave algorithm computes an effective channel transmittance between two adjacent pressure levels as

$$\langle \tau(P_1, P_2) \rangle = \exp\left[-(\alpha + \beta\rho_V + \gamma\rho_L)\right] \qquad (4\text{-}1)$$

where ρ_V is the water vapor column density of the (P_1, P_2) layer, ρ_L is its liquid water column density, and the coefficients α, β, γ, are calculated for each layer and channel. They implicitly depend on temperature, pressure, and the angle of observation; β also depends implicitly on ρ_V. For channel 15, α has a weak dependence on the local geomagnetic field. The magnetic field is calculated by a fifth-order spherical-harmonic representation that has an accuracy of a few microteslas. The coefficient α includes the opacity due to O_2 and a small contribution from pressure-induced absorption by N_2. Parameterization of the coefficients uses approximations described by Rosenkranz (2003) for oxygen-band or window-type channels. In the oxygen band, effective layer opacities are represented by a polynomial in temperature. The opacity profile is computed on a set of fixed pressure levels and then linearly interpolated to the pressure levels of the retrieval, which can be variable (as is the case for the surface pressure). Window-channel coefficients use analytic approximations for far-wing line and continuum absorption. Channels near the two water lines (channels 1 and 18-22) use a Lorentzian-line calculation for the nearby line, with the contributions of other lines treated in the same way as for a window. The local water-line parameters, the water continuum, and the liquid-water absorption are interpolated from a table as functions of temperature.

The retrieval algorithm described in Section 5 also makes use of the derivatives $d\alpha/dt$ and $d\beta/d\rho_V$, which are computed in the rapid algorithm by appropriate analytic expressions corresponding to the local-line and continuum components.

The transmittance of multiple layers is calculated by taking the product of the transmittances for each layer. This transmittance is then used in the radiative transfer equation to compute brightness temperature:

$$\Theta = \int_0^{P_s} T(P) < d\tau(0,P) > + \varepsilon T_s < \tau(0,P_s) > + (1-\varepsilon) < \tau(0,P_s) > \int_0^{P_s} T(P) < d\tau(P_s,P) > + (1-\varepsilon)\Theta_c < \tau(0,P_s) >^2 \tag{4-2}$$

where Θ_{TOA} is the brightness temperature emitted from the top of the atmosphere, $\tau(0,P_S)$ is the one-way transmittance of the atmosphere,

$$\Theta_{direct} = \int_0^{P_S} T(P) < d\tau(0,P) > \tag{4-3}$$

is the component of brightness temperature emitted from the atmosphere on a direct path to space, Θ_S is the surface brightness (emissivity times temperature),

$$\Theta_{sky} = \int_0^{P_S} T(P) < d\tau(P_S,P) > + \Theta_c < \tau(0,P_S) > \tag{4-4}$$

is the sky brightness temperature (including the attenuated cosmic contribution) as it would be observed from the surface, and T_S is the physical surface temperature. T(P) is

atmospheric temperature at level P, P_S is the surface pressure, and Θ_c is the cosmic background brightness temperature. The form of (4-2) allows separation of the estimation of surface brightness from the estimation of temperature, as described in Section 5.

Θ_{sky} is computed for a zenith angle θ_{ref} which, due to surface scattering, in general differs from the zenith angle θ for the direct path from surface to satellite. When the surface is classified (see section 5) as either water or coastline, the ratio $\rho_s = \sec(\theta_{ref})/\sec(\theta)$ is estimated as part of the retrieval solution, as described in section 5. For all other surface types, surface scattering is assumed to be Lambertian, and is approximated by

$$\sec(\theta_{ref}) = 1.55 - 0.16 \ln(\kappa_0 + 0.06) \qquad (4\text{-}5)$$

where $\kappa_0 = -\ln(\tau_{zenith}(0,P_S))$is the opacity of the atmosphere at zenith.

Planck's equation for radiant intensity is a nonlinear function of temperature. For microwave frequencies, however, the physical temperatures encountered in the earth's atmosphere lie at the high-temperature asymptote of this function. Hence, as discussed by Janssen (1993), brightness temperature can be used as a surrogate for radiance in the equation of radiative transfer with an accuracy of a few hundredths of a Kelvin, provided that the cosmic background is assigned an effective brightness temperature at frequency ν of

$$\Theta_C = \frac{h\nu}{2k} \times \frac{e^{h\nu/kT_C} + 1}{e^{h\nu/kT_C} - 1} \qquad (4\text{-}6)$$

instead of its actual temperature $T_C = 2.73$ K, in order to linearize Planck's function.

Figures 11 and 12 show the derivatives of transmittance with respect to a vertical coordinate which is the logarithm of integrated water vapor for the channels sensitive to moisture, and the logarithm of pressure (a surrogate for integrated oxygen content) for channels in the oxygen band. These weighting functions indicate the atmospheric layers from which the thermal emission measured by each channel originates.

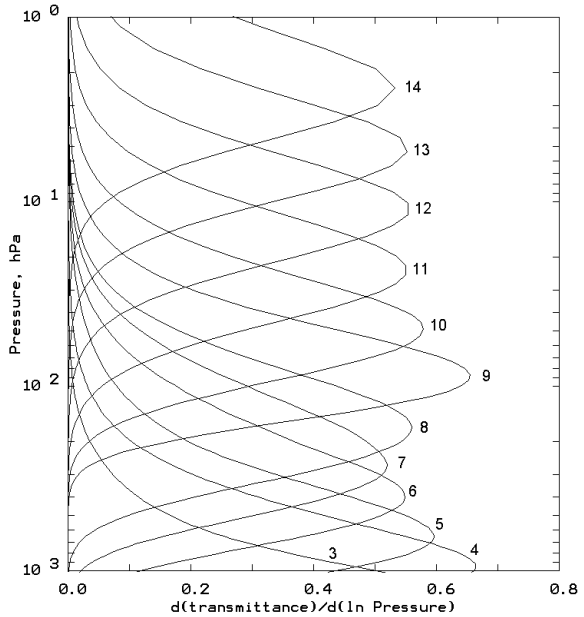

Figure 11. Oxygen Band Weighting Functions for Unit Surface Emissivity (channel numbers are for AMSU-A = ATMS numbers -1)

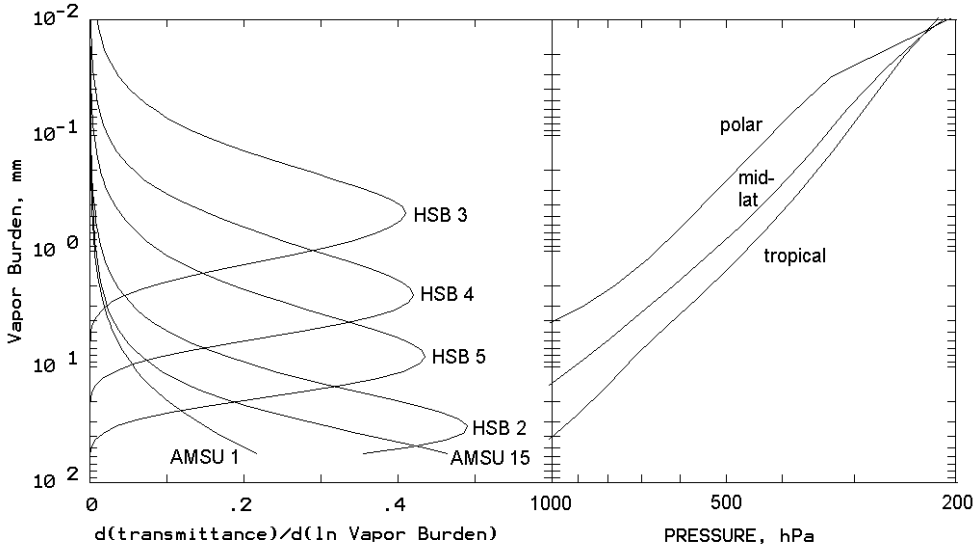

Figure 12. Water Vapor Weighting Functions for Unit Surface Emissivity (left – illustrated for HSB; ATMS channels are nearly identical and fills gaps between HSB channels) and Vapor Burden vs. Pressure in Three Different Climatologies (right)

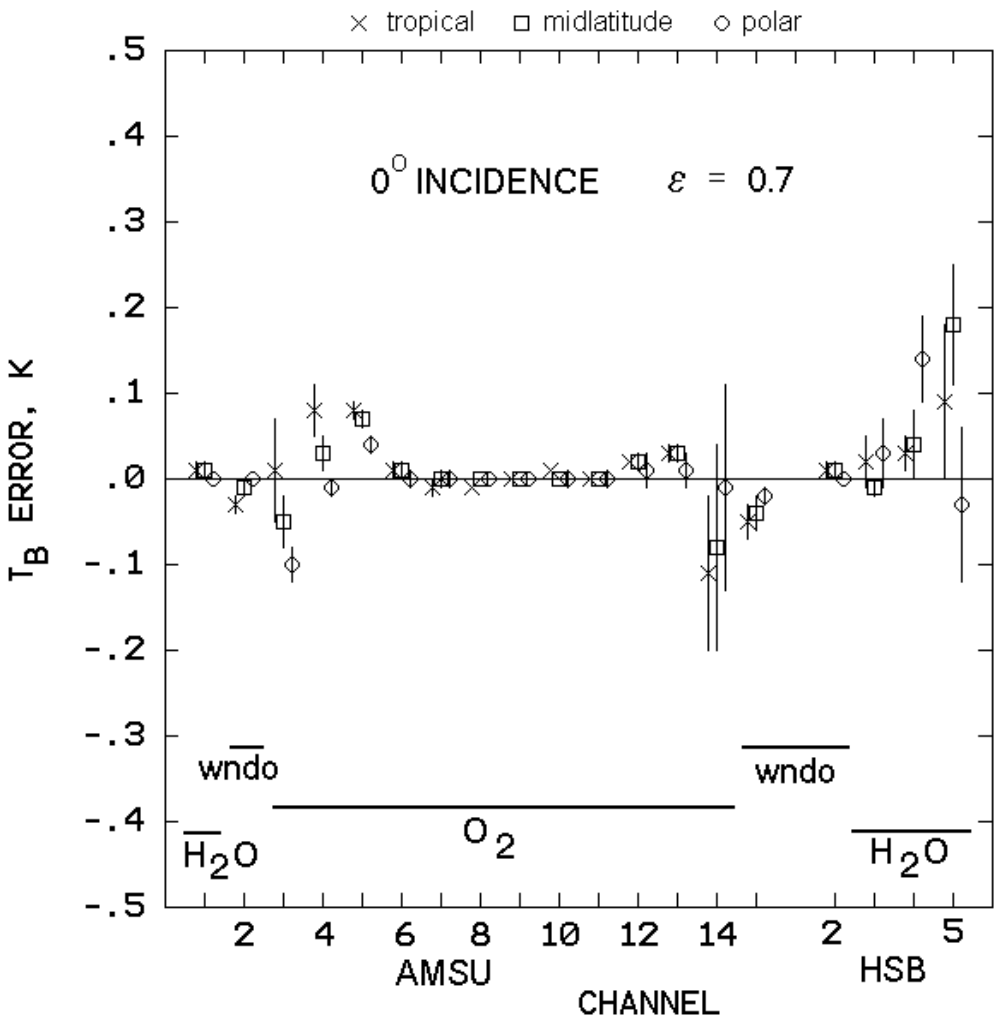

Figure 13. Brightness Temperature Errors (Rapid Algorithm Minus Line-by-Line Algorithm) for AMSU and HSB Channels. Results are nearly identical for ATMS channels. Vertical Lines Indicate ± 1 Standard Deviation; ε is the Surface Emissivity.

The ability of the rapid algorithm to approximate a line-by-line calculation was tested on a set of 300 profiles from the TOVS Initial Guess Retrieval (TIGR) (Chedin, *et al*., 1985) ensemble. The first 100 profiles from each of the tropical, mid-latitude, and polar groups were used. Figure 13 shows brightness temperature errors (mean ± 1 standard deviation) at nadir, with surface emissivity = 0.7. For the channels that are not opaque (1-5, 15-17, 19 and 20), these brightness temperature errors depend on surface emissivity. The value ε = 0.7 is typical of ocean at the highest frequencies, and intermediate between ocean and land at the lowest frequencies. Errors for higher-emissivity land surfaces are smaller than in Figure 13. The errors for channel 14 include the consequences of the magnetic field approximation. The output files contain a flag structure, MW_tair_range, which indicates whether the final temperature at any pressure level > 0.1 hPa lies outside of the range of profiles for which the rapid algorithm has been found to reproduce a line-by-line calculation within the instrument sensitivity. Different bits are set for temperatures outside the validated range by <10%, 10 to 25%, or >25%.

5. Microwave Surface Brightness Model

The surface brightness temperature spectrum Θ_S is modeled by a six-parameter (T_0 , T_1 , T_2 , ν_1 , ν_2 , s) curve, added to an *a priori* surface brightness

$$\Theta_S(\nu) = \varepsilon_0(\nu)\, T_{S0} + T_0 + T_1\, \nu^s / (\nu^s + \nu_1^s) + T_2\, \nu^s / (\nu^s + \nu_2^s) \qquad (4\text{-}7)$$

where $\varepsilon_0(\nu)$ is a preliminary estimate of emissivity for the surface type obtained from the classification algorithm described in section 5, and T_{S0} is the *a priori* (climatological) surface temperature. The parameters T_0 , T_1 , T_2 are used in the retrieval solution to adjust the spectrum (they have *a priori* values of zero), while ν_1 , ν_2 and s are assigned according to surface type, as in Table 2. The last three terms in (4.1.7) also help to correct for effects such as ocean surface roughness, errors in the dielectric constant model, misclassification of the surface, or errors in the estimated land fraction within the footprint.

In Figure 14, the rapid transmittance algorithm is tested against measurements made by the AMSU-A on the NOAA-15 satellite (see Rosenkranz, 2003) and the HSB on Aqua (see Rosenkranz and Barnet, 2006). The calculated brightness temperatures are based on coincident radiosonde profiles, using window channels to infer the surface emissivity, as described in section 5. Sidelobe corrections from Mo (1999) were applied to the AMSU-A measurements in the figure, but no corrections were made to the HSB measurements. Performance for ATMS is nearly identical.

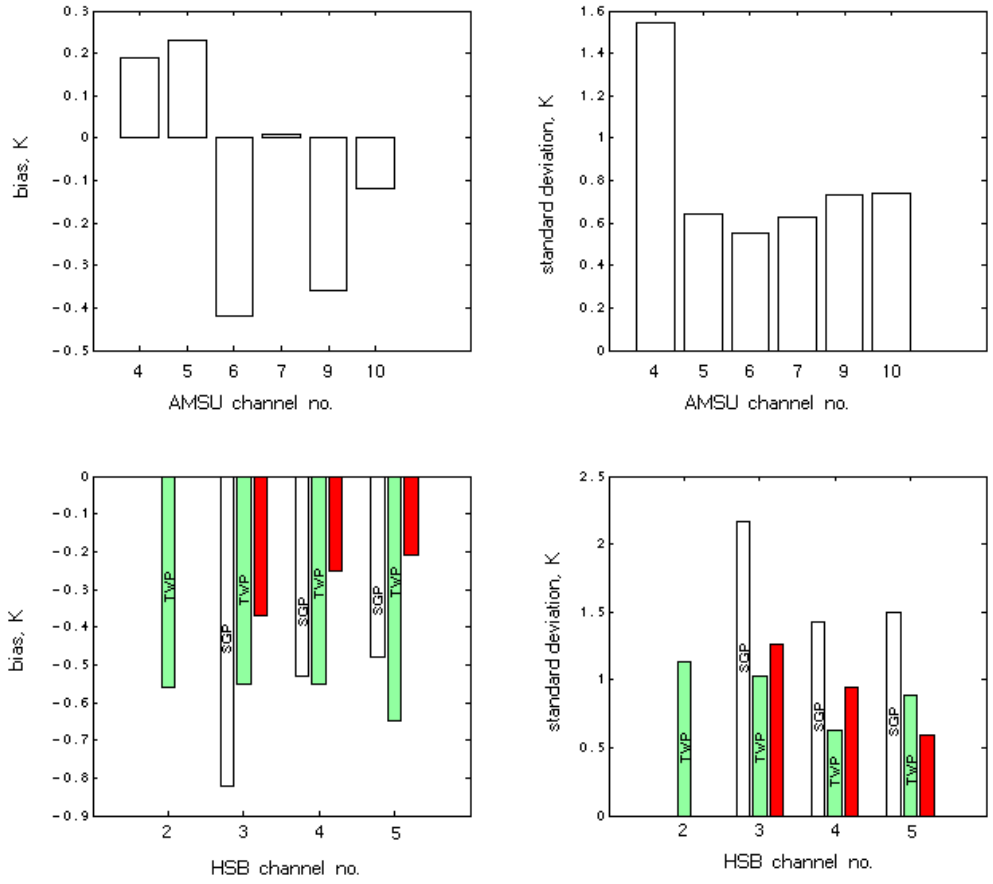

Figure 14. Statistics of differences between measured brightness temperatures minus brightness temperatures calculated from radiosonde profiles. Three profile ensembles are shown for HSB. Performance for ATMS is nearly identical.

5. Retrieval Algorithms

Profile Retrieval Algorithm

The microwave profile retrieval algorithm derives temperature, water vapor and non-precipitating cloud liquid water profiles from ATMS brightness temperatures. This is an iterative algorithm in which the profile increments are obtained by the minimum-variance method, using weighting functions computed for the current temperature and moisture profiles with the rapid transmittance algorithm described in Section 4.1. A block diagram is shown in Figure 15.

The input vector of measured brightness temperatures is accompanied by an input validity vector whose elements are either one or zero. This provides a way of handling missing or bad data.

1 Preliminary Surface Type Classification

The surface classification algorithm is diagrammed in Figure 16. The classification rules are from Grody, *et al.,* (2000), and make use of discriminant functions that are linear combinations of channels 1, 2, 3, and 16. If sea ice is indicated by the classification algorithm, then its concentration fraction is estimated from a linear operation on channels 1, 2, and 3. If the surface type is glacier or snow-covered land, then the snow or ice fraction is estimated using channels 3 and 16. Parameters of the surface brightness model (Equation 4.1.7) are assigned according to surface type as in Table 2. *A priori* emissivities for the ice and snow types were estimated from NOAA-15 and Aqua data. For land, $\varepsilon_0(\nu) = 0.95$ at all frequencies; for seawater, the dielectric constant model of Ellison, *et al.,* (2003) was used to compute the emissivity of a flat surface viewed in the polarization of the ATMS radiometer.

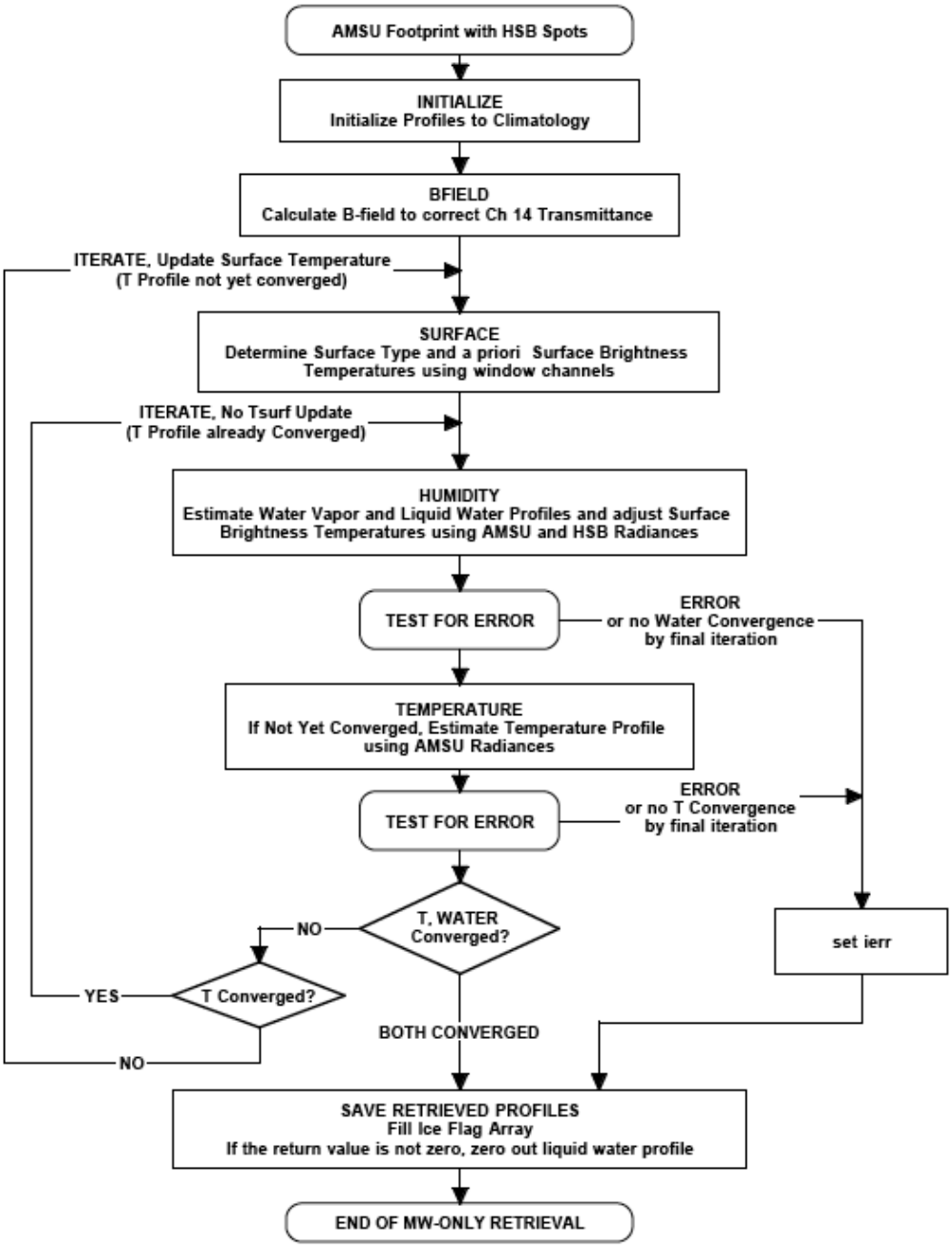

Figure 15. ATMS Profile Retrieval

(Note: For "AMSU-A" and AMSU-A and HSB" in the figure, substitute "ATMS")

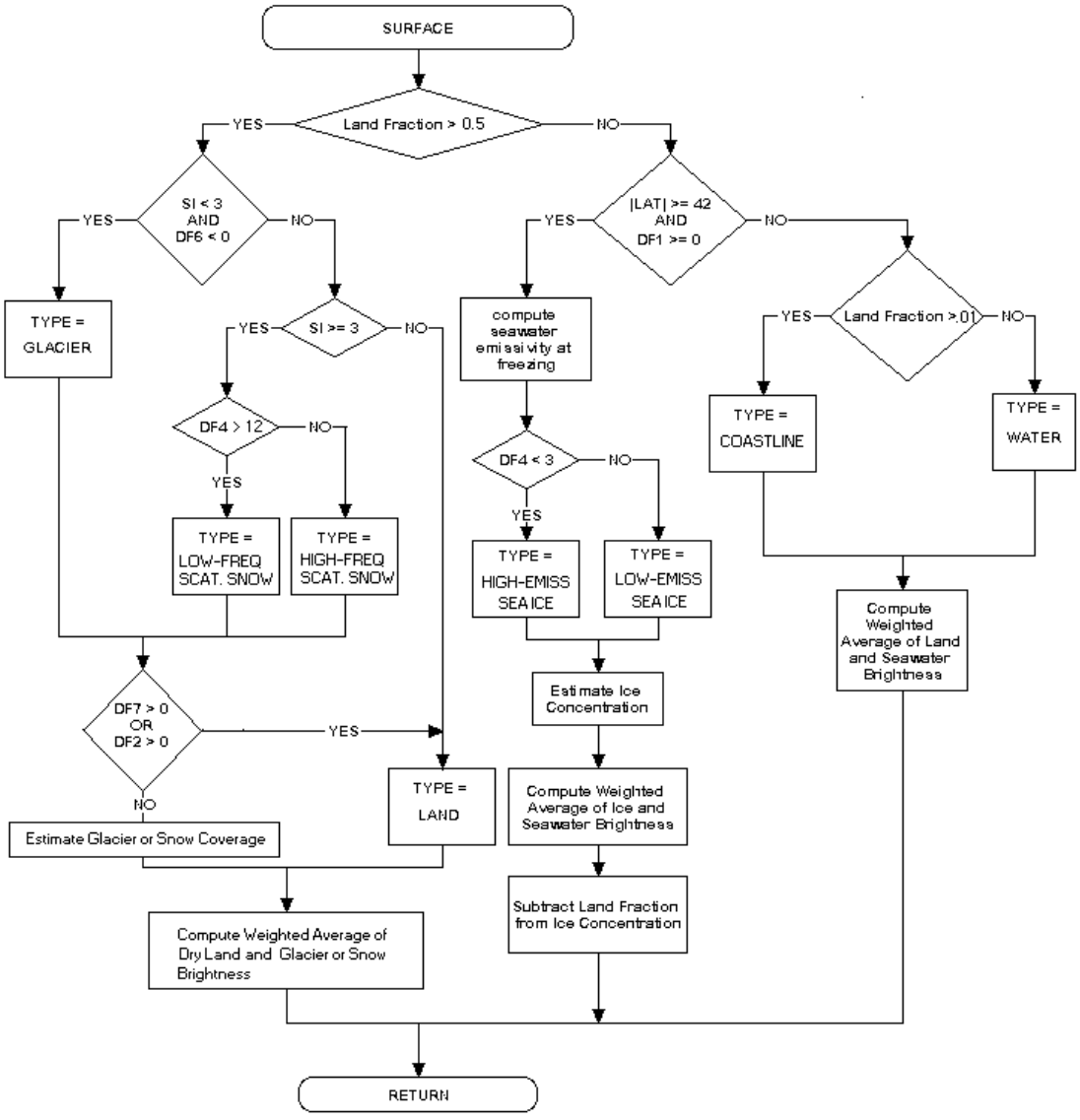

Figure 16. Surface Classification Algorithm

2 Atmospheric Moisture and Condensation Model

Measurements of brightness temperature at the ATMS frequencies are a result of the vertical profile of atmospheric opacity relative to temperature and hence do not by themselves distinguish, at any given altitude, between opacity due to water vapor and opacity due to liquid water. However, the physics of water vapor condensation add some *a priori* information or constraints. Wilheit (1990) suggested that liquid water should be placed at the altitudes where the measurements force relative humidity into saturation. Although the water vapor profile is saturated within the cloudy part of the field of view, it is assumed here that the condensation process is not spatially resolved, hence the threshold for condensation, denoted by H_L, may be less than 100%. The saturation vapor pressure depends on temperature, and due to errors in the estimated temperature profile, H_L may

also be greater than 100%. Therefore, H_L is retrieved as an atmospheric parameter, along with a profile H, which is a generalization of relative humidity to encompass both vapor and liquid water, as illustrated in Figure 17. It is important to note that because convergence is determined from the brightness temperature residuals, which, in turn, are computed using the vapor and liquid mixing ratios (or column densities), the role of H in this algorithm is only to introduce the *a priori* statistics and constraints.

The average vapor mixing ratio in the field of view is

$$\rho_V = \rho_S [\text{ramp}(H, 10) - f(H)] / 100 \quad (5\text{-}1)$$

where ρ_S is the saturation value of mixing ratio,

$$\text{ramp}(x,c) = \begin{cases} x & \text{for } x \geq c; \\ c \exp(x/c - 1) & \text{for } x < c, \end{cases} \quad (5\text{-}2)$$

and

$$f(H) = \text{ramp}(H - H_L, 6) \quad (5\text{-}3)$$

Thus, the value of ρ_V / ρ_S lies between zero and $H_L/100$. The liquid water mixing ratio averaged over the field of view is assumed to be given by

$$\rho_L = c_1 f(H) \quad (5\text{-}4)$$

where c_1 is a coefficient equivalent to a liquid/air mass mixing ratio of 10^{-5} per percent. The saturation vapor mixing ratio is computed from the temperature profile by the formula of Liebe (1981). Saturation is calculated with respect to liquid water (by extrapolation) even when the temperature is below 273 K. This model therefore allows supercooled liquid water and water vapor greater than the saturation value with respect to ice.

Table 2. Surface-Model Parameters Fixed by Classification. (□0, 1, 2, □□□HL = a priori standard deviation of T0, T1, T2, p□, HL)

Surface type	s	ν_1 (GHz)	ν_2 (GHz)	σ_0 (K)	σ_1 (K)	σ_2 (K)	σ_ρ	σ_{HL}(%)
0. Coastline	1.2	90	-	note 1	note 1	0	0.12	8
1. Land	1.2	90	-	15	20	0	0	8
2. Water	1.5	50	-	note 1	note 1	0	0.12	8
3. High-emissivity sea ice	3	40	120	10	10	10	0	0
4. Low-emissivity sea ice	3	40	120	10	10	10	0	0
5. Snow (high-frequency scattering)	3	50	150	20	20	20	0	0
6. Glacier/snow (very low-frequency scattering)	3	40	120	20	20	20	0	0
7. Snow (low-frequency scattering)	3	33	90	20	20	20	0	0

Note 1: For water or coastline, $\sigma_0^2 = 25 + (0.55\ T_s\ \sigma_{LF})^2$ and $\sigma_1^2 = 100 + (0.25\ T_s\ \sigma_{LF})^2$, where σ_{LF} is the estimated uncertainty in the land fraction.

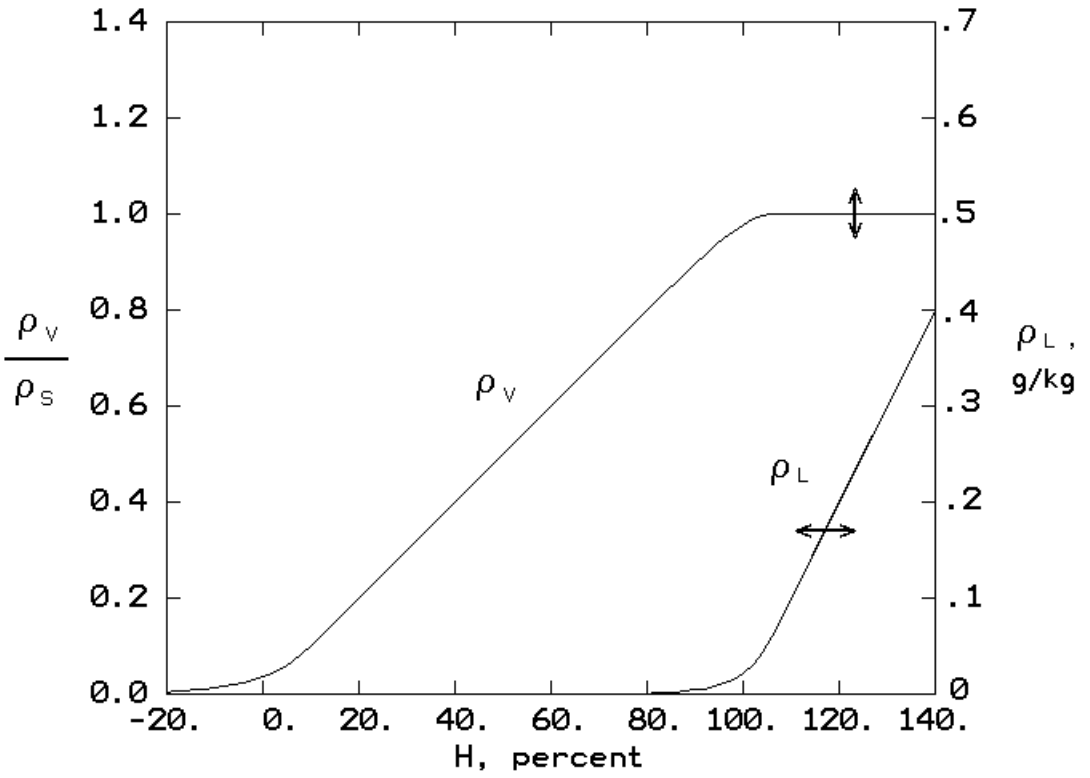

Figure 17. Water Vapor(□v) and Cloud Liquid (□L) Mixing Ratios as Functions of HL = 100. The Arrows Indicate How the curves Change as HL Varies

3 Estimation of Surface Brightness and Atmospheric Moisture

This part of the algorithm is based on retrieval methods described by Wilheit (1990), Kuo, *et al*., (1994), Wilheit and Hutchison (1997), and Rosenkranz (2006). It uses channels 1, 2, 3, 16and 18-22. The H profile, H_L, and four surface parameters T_0, T_1, T_2, and p_ρ are concatenated into a vector **Y**. The parameter p_ρ, when the surface type is either water or coastline, determines the secant ratio ρ by

$$\rho = \sec(\theta_{ref})/\sec(\theta) = 1 + \text{ramp}(p_\rho, 0.02) \quad (5\text{-}5)$$

The cost function to be minimized is

$$(Y_{est}-Y_o)^T \mathbf{S}_Y^{-1} (Y_{est}-Y_o) + (\Theta_{obs}-\Theta-\Theta')^T (\mathbf{S}_e+\mathbf{S}_f)^{-1} (\Theta_{obs}-\Theta-\Theta') \quad (5\text{-}6)$$

in which Y_{est} is the estimate of Y, Y_o is its *a priori* value and $\mathbf{S}_Y$ is its covariance matrix with respect to Y_o, Θ_{obs} is a vector of the eight measured antenna temperatures, $\mathbf{S}_e$ is their error covariance matrix (assumed to be diagonal), Θ' is the tuning correction for sidelobe effects and possible transmittance error, and Θ is a brightness temperature vector computed from the current values of temperature, moisture, and surface brightness. $\mathbf{S}_f$ is a diagonal covariance matrix which approximately represents errors in Θ resulting from errors in the temperature profile retrieval and tuning.

The estimate of Y is obtained by Newtonian iteration (see Rodgers, 1976), except that Eyre's (1989) method of damping is used to avoid large relative humidity increments, because of the nonlinearity of the problem:

$$Y_{est_n} = Y_{est_{n-1}} - \delta [Y_{est_{n-1}} - Y_o] + \delta \mathbf{S}_Y \mathbf{W}_Y^T X_Y \quad (5\text{-}7)$$

in which $(\mathbf{W_Y})_{ij} = \partial\Theta_i/\partial Y_j$, superscript T indicates transpose, and X_Y is the solution vector to

$$[\mathbf{W}_Y \delta \mathbf{S}_Y \mathbf{W}_Y^T + \mathbf{S}_e + \mathbf{S}_f] X_Y = \Theta_{obs} - \Theta - \Theta' + \mathbf{W}_Y \delta [Y_{est_{n-1}} - Y_o] \quad (5\text{-}8)$$

where

$$\delta = \begin{cases} 1.0 \text{ if } (\Theta_{i_{obs}} - \Theta_i - \Theta') < 10 \text{ K for all channels i, or } n \geq 10; \\ 0.1 \text{ otherwise.} \end{cases} \quad (5\text{-}9)$$

Here δ is a scalar rather than a matrix as in Eyre's paper. The Jacobian matrix $\mathbf{W}_Y$ is computed for the state represented as $Y_{est_{n-1}}$ by application of the chain rule for differentiation to the forward model equations. This is sometimes referred to as a "tangent linear" method. For example, the elements of $\mathbf{W}_Y$ corresponding to H values are

$$\frac{\partial\Theta}{\partial H} = G \bullet \left(\frac{\partial\kappa}{\partial\rho_v} \bullet \frac{\partial\rho_v}{\partial H} + \gamma \frac{\partial\rho_L}{\partial H} \right) \quad (5\text{-}10)$$

in which $G = \partial\Theta/\partial\kappa$ where κ represents the opacity of the layer at the viewing angle, and $\gamma = \partial\kappa/\partial\rho_L$. G is equal to the integral over an atmospheric layer of the function G(h) for which an expression is given by Schaerer and Wilheit (1979). The rapid transmittance algorithm computes the coefficient γ in the small-droplet (Rayleigh) approximation. Hence, it is intended to be applied only to non-precipitating cloud situations. Differentiation of (5-1) and (5-4) yields $\partial\rho_v/\partial H$ and $\partial\rho_L/\partial H$.

The elements of $\mathbf{S}_Y$ corresponding to relative humidity were calculated from the TIGR profile ensemble (Chedin, *et al*., 1985). For the surface, it is necessary to postulate statistics based on physical plausibility and observed ranges of variation. The standard deviations of parameters depend on surface type, and are listed in Table 2. The *a priori* relative humidity is obtained from climatological databases (NCEP 50-year reanalysis, Kistler, *et al*., 2001) of temperature and vapor mixing ratio, but limited to < 90%. Hence the initial cloud liquid-water profile always has very small values. The *a priori* values of T_0, T_1 and T_2 are set to zero, and H_L to 100, in all cases; the *a priori* value of p_ρ is assumed to be 0.02. For water surfaces, the parameters T_0, T_1, and p_ρ are all related to roughness, and therefore the *a priori* statistics assigned to them assume correlation coefficients of 0.2. As indicated by the standard deviations in Table 2, at most three of the four surface-roughness parameters are allowed to vary for any surface type.

After update of Y by (5-7 and 5-8), the water vapor and liquid water profiles are computed from (5-4), and surface brightness is computed for both window and sounding frequencies from (4-7), using the new estimate.

4 Estimation of Temperature Profile

The atmospheric temperature vector is augmented by T_S, which is considered to be distinct from the air temperature near the surface. The measured Θ's used in the temperature profile retrieval are channels 4-15. Given an existing estimate $T_{est_{n-1}}$, the new estimated profile is to be determined from a vector Θ_{obs} of observed brightness temperatures. A cost function similar to (5-6), with Y replaced by T, is to be minimized separately for the temperature profile. Hence, the retrieved profiles are not influenced by statistical correlations between temperature and relative humidity.

Initially, the temperature profile, including surface temperature, is set to a climatological profile T_o which depends on latitude and season. The new, minimum-variance estimate of T is obtained by Newtonian iteration (Rodgers, 1976, eq. 101):

$$T_{est_{n-1}} = T_o + \mathbf{S_T}\,\mathbf{W_T}^{\mathbf{T}}\,X_T \qquad (5\text{-}11)$$

where S_T is the temperature covariance matrix and X_T is the solution vector to

$$[\mathbf{W}_T\,\mathbf{S}_T\,\mathbf{W}_T{}^T + \mathbf{S}_e + \mathbf{S}_f]\,X_T = \Theta_{obs} - \Theta - \Theta' + \mathbf{W}_T\,[\,T_{est_{n-1}} - T_o\,] \qquad (5\text{-}12)$$

The error covariance matrix ($\mathbf{S}_e$+$\mathbf{S}_f$) includes the effects of surface brightness uncertainty, water vapor, liquid water, and instrument noise.

The elements of the Jacobian matrix $\mathbf{W}_T$ corresponding to the atmospheric part of the temperature vector are given by

$$\partial\Theta/\partial T = K + G\,\partial\kappa/\partial T \qquad (5\text{-}13)$$

where K is equal to the temperature weighting function as defined by Schaerer and Wilheit (1979) integrated over the given atmospheric layer, $G = \partial\theta/\partial\kappa$, and $\partial\kappa/\partial T$ is computed by the rapid transmittance algorithm. The second term on the right side of (5-13) is a small correction to the temperature weighting function.

The elements of $\mathbf{W}_T$ corresponding to T_S are obtained by partial differentiation of Eq. (4-2):

$$\frac{\partial\Theta}{\partial T_s} = \frac{\tau\,\Theta_{sky}\,\Theta_s}{T_s^2} \qquad (5\text{-}14)$$

The dependence on T_S is nonlinear here because Θ_S is considered to be a known input from the moisture algorithm. If the validity of a channel is zero, then the row of $\mathbf{W}_T$ corresponding to that channel is set to zeros. The dimensions of the matrix remain the same.

The covariance of the temperature vector was computed from the TIGR ensemble (Chedin, *et al*., 1985). T_S is assumed to have the same *a priori* mean and variance as the air temperature near the surface, but the covariances of T_S with atmospheric temperatures are assumed to be reduced by a factor of 0.9 from those of the surface air temperature.

5 Iteration Procedure and Convergence Tests

After the temperature profile is updated using (5-11and 5-12), the algorithm returns to the moisture and surface-brightness section for another iteration of (5-7 and 5-8), using weighting functions computed for the updated temperature and moisture profiles. Convergence is tested separately for the temperature channels and for the moisture/surface channels; iteration of either part of the algorithm is suspended when one of the following conditions is met: (1) the computed brightness temperature vector Θ meets the closure criterion

$$\sum_{i=1}^{N_B} \frac{\left[\Theta_{obs_i} - \Theta_i - \Theta_i'\right]^2}{\Delta T_i^2} \leq N_B \qquad (5\text{-}15)$$

where ΔT_i is the instrument noise (not the total measurement error) on channel i and N_B is the number of valid elements in Θ_{obs}; or (2) when successive computations of the left side of (5-15) change by less than 1% of the right side, for the temperature channels, or 2% for the moisture/surface channels; or (3) when the number of iterations exceeds a preset limit, which is 12 for the temperature channels and 16 for the moisture/surface channels. Typically, iteration of the temperature profile ceases after one or two iterations, but the moisture profile often requires six or more iterations.

6 Output Flags

Several error flags are produced by the microwave retrieval algorithm. The 'mw_ret_code' may contain any of the following values (or sums of values if more than one condition applies):

0: No error.

1: Moisture variables rejected. Test of residuals for channels 1-9,16 and 18-22.

2: Troposphere temperature profile rejected. Test of residuals for moisture-related channels when integrated vapor > 6 mm or integrated cloud liquid > 0.1 mm, or for channels 4-9 under any conditions.

4: Integrated cloud liquid water > 0.5 mm.

8: Insufficient valid channels to do the retrieval.

32: Derived surface emissivity > 1 for anyfrequency.

64: Stratosphere temperature profile rejected. Test of residuals for channels 10-15.

In polar regions, error value 1 may occur without 2, and is then considered nonfatal.

The Qual_MW_Only_Temp_Tropo flag is a summary of the bits in mw_ret_code that affect the tropospheric temperature quality (2, 4, 8, 32) and can have values 0: usable, or 2: not usable.

The Qual_MW_Only_Temp_Strat flag is a summary of the bits in mw_ret_code that affect the stratospheric temperature quality (8, 64) and can have values 0: usable, or 2: not usable.

The Qual_MW_Only_H2O flag is a summary of the bits in mw_ret_code that affect the moisture variables (1, 4, 8, 32). Possible values are 0: moisture profiles and integrals usable; 1: only integrals usable; 2: not usable.

If the mean square of brightness temperature residuals for the water vapor channels is greater than 64 (i.e., 8K rms per channel), then an ice-scattering flag ('cloud_ice') is set at all altitudes for which clouds are present and the temperature estimate is below 273 K. This typically flags intense precipitation systems like thunderstorms.

7 Precipitation Flags

The objective of the flags for each of channels 5-9 is to alert users of this data to the possibility that retrievals based on these microwave channels might be impacted by precipitation. The four possible flag states are:

0 The magnitude of the detected precipitation perturbations (if any) are less than 0.5 K

1 Small perturbations are present (nominally between 0.5 and 2 K), which are approximately correctable

2 Estimated precipitation-induced brightness temperature perturbations for this channel may exceed 2 K in magnitude, so perturbation corrections are less reliable

-1 It is unknown whether perturbations due to precipitation are present (e.g., surface elevation >2 km)

6. Input Quality Control and Ancillary Products

Quality Control

Key to the quality of the Level 2 products is careful quality control of the calibrated radiances. ATMS data is screened for the following problems:

1) Instrument State is not 0 (Process)
   Any state other than process indicates data is missing or bad.

2) BT > 350 K or BT < 50 K

If any channel is out of bounds, the entire FOV is discarded.

Background Climatology

A background climatology “Clim” is available on a 2.5 degree mercator grid using 100 levels. The climatology is based on two files: "NCEP" and "UARS."

"NCEP" has temperature profiles from the surface to 100 mb and water profiles from the surface to 300 mb as monthly means derived from the 20 year (1979-1998) reanalysis on a 2.5 degree mercator lat/lon grid.

"UARS" has temperature, water vapor and ozone month means and zonal (latitude) means. The information below 100 mbar comes from the NCEP reanalysis, above 100 mbar from the microwave limb sounders (UARS and MLS).

The PGE fills its climatology from these two files as:

1) Temperature profile:

   a) below 100 mbar from NCEP, tri-linearly interpolated by month,

      lat, lon and then log-pressure interpolated onto the 100 levels.

   b) above 100 mbar Temp is extrapolated using P**4 extrapolation

2) H_2O profiles. From the “NCEP” file below 300 mb, tri-linearly interpolated by month, lat, lon. Above 300 mb the "UARS" file is used, linearly interpolated between two latitude zones.

AVN Forecast PSurf

The AVN forecast surface pressure, PSurf, is used by the L2 retrieval. The surface pressure is available on a one-degree grid. The surface pressure is calculated from the 3-, 6-, and 9-

hour forecasts from the same model run, interpolated in space and time to match observed location.

Clim T profile is used in the calculation of Psurf when AVN is not available.

7. References

Bauer, A., Godon, M., Kheddar, M., and Hartmann, J.M., 1989: Temperature and Perturber Dependences of Water Vapor Line-Broadening. Experiments at 183 GHz; Calculations Below 1000 GHz, *J. Quant. Spectrosc. Radiat. Transfer*, **41**, 49-54.

Bauer, A., Godon, M., Carlier, J., and Ma, Q., 1995: Water Vapor Absorption in the Atmospheric Window at 239 GHz, *J. Quant. Spectrosc. Radiat. Transfer*, **53**, 411-423.

Bauer, A., Godon, M., Carlier, J., Ma, Q., and R.H. Tipping, 1993: Absorption by H_20 and H_20-N_2 Mixtures at 153 GHz, *J. Quant. Spectrosc. Radiat. Transfer*, **50**, 463-475.

Chedin, A., N. A. Scott, C. Wahiche, and P. Moulinier, 1985: The improved initialisation inversion method: A high resolution physical method for temperature retrievals from the TIROS-N series. *J. Clim. Appl. Meteor.*, **24**, 128-143.

Ellison, W. J., S. J. English , K. Lamkaouchi, A. Balana, E. Obligis, G. Deblonde, T. J. Hewison, P. Bauer, G. Kelly and L. Eymard, 2003: "A comparison of ocean emissivity models using the Advanced Microwave Sounding Unit, the Special Sensor Microwave Imager, the TRMM Microwave Imager, and airborne radiometer observations," *J. Geophys. Res.*, **108**(D21), 4663, doi:10.1029/2002JD003213.

Eyre, J. R., 1989: Inversion of cloudy satellite sounding radiances by nonlinear optimal estimation. I: Theory and simulation for TOVS. *Q. J. R. Meteorol. Soc.* , **115**, 1001-1026.

Gamache, R.R., J.-M. Hartmann, and L. Rosenmann, 1994: Collisional broadening of water vapor lines- 1. A survey of experimental results. *J. Quant. Spectrosc. Radiat. Transfer*, **52**, 481-499.

Godon, M., Carlier, J. and Bauer, A., 1992: Laboratory Studies of Water Vapor Absorption in the Atmospheric Window at 213 GHz, *J. Quant. Spectrosc. Radiat. Transfer*, **47**, 275-285.

Grody, N., F. Weng, and R. Ferraro, 2000: "Application of AMSU for obtaining hydrological parameters." In *Microwave Radiometry and Remore Sensing of the Earth's Surface and Atmosphere*, (P. Pampaloni and S. Paloscia, eds.) VSP (ISBN 90-6764-318-1), pp. 339-352.

Janssen, M.A. (ed.), 1993: *Atmospheric Remote Sensing by Microwave Radiometry*, Chap. 1, New York: Wiley.

Kistler, R., E. Kalnay, W. Collins, S. Saha, G. White, J. Woollen, M. Chelliah, W. Ebisuzaki, M. Kanamitsu, V. Kousky, H. van den Dool, R. Jenne, and M. Fiorino, 2001: "The NCEP-NCAR 50-Year Reanalysis: Monthly Means CD-ROM and Documentation," *Bull. Am. Meteor. Soc.* **82**, 247-267.

Kuo, C. C., D. H. Staelin and P. W. Rosenkranz, 1994: "Statistical Iterative Scheme for Estimating Atmospheric Relative Humidity Profiles," *IEEE Trans. Geosci. and Remote Sensing* , **32**, 254-260.

Liebe, H.J. and Dillon, T.A., 1969: Accurate Foreign-Gas-Broadening Parameters of the 22-GHz H20 Line from Refraction Spectroscopy, *J. Chem. Phys.*, **50**(2), 727-732 (1969).

Liebe, H.J., Thompson, M.C. Jr., and Dillon, T.A., 1969: Dispersion Studies of the 22 GHz Water Vapor Line Shape, *J. Quant. Spectrosc. Radiat. Transfer*, **9**, 31-47.

Liebe, H. J., 1981: "Modeling attenuation and phase of radio waves in air at frequencies below 1000 GHz," *Radio Sci*., **16**, 1183-1199.

Liebe, H.J., and Layton, D.H., Millimeter-Wave Properties of the Atmosphere: Laboratory Studies and Propagation Modeling, NTIA Report 87-224, October 1987.

Liebe, H.J., Hufford, G.A., and Manabe, T., 1991: A Model for the Complex Permittivity of Water at Frequencies Below 1 THz, *Int. J. of Infrared and Mill. Waves,* **12**(7), pp. 659-675.

Liebe, H.J., Rosenkranz, P.W., and Hufford, G.A., 1992: Atmospheric 60-GHz Oxygen Spectrum: New Laboratory Measurement and Line Parameters, *J. Quant. Spectrosc. Radiat. Transfer*, **48**(5/6), 629-643.

Liebe, H.J., G.A. Hufford, and M.G. Cotton, 1993: Propagation Modeling of Moist Air and Suspended Water/Ice Particles at Frequencies Below 1000 GHz, in *AGARD Conference Proceedings 542*, *Atmospheric Propagation Effects through Natural and Man-Made Obscurants for Visible to MM-Wave Radiation*, pp.3.1-3.10.

Mo, T., "AMSU-A antenna pattern corrections," *IEEE Trans. Geosci. Rem. Sens.*, **37**, 103-112 (1999).

Poynter, R.L. and Pickett, H.M., 1985: Submillimeter, Millimeter, and Microwave Spectral Line Catalog, *Applied Optics*, **24**(14), pp. 2235-2240.

Rodgers, C. D., 1976: Retrieval of atmospheric temperature and composition from remote measurements of thermal radiation. *Rev. Geophys. and Space Phys*., **14**, 609-624.

Rothman, L. S., C. P. Rinsland, A. Goldman, S. T. Massie, D. P. Edwards, J.-M. Flaud, A. Perrin, C. Camy-Peyret, V. Dana, J-Y. Mandin, J. Schroeder, A. McCann, R. R. Gamache, R. B. Wattson, K. Yoshino, K. V. Chance, K. W. Jucks, L. R. Brown, V. Nemtchinov, P. Varanasi, 1998: "The HITRAN Molecular Spectroscopic Database and HAWKS (HITRAN Atmospheric WorKStation):1996 Edition," *J. Quant. Spectrosc. Radiat. Transfer* **60**, 665-710.

Rosenkranz, P. W., 1998: Water vapor microwave continuum absorption: A comparison of measurements and models. *Radio Science*, **33**, 919-928. (Correction, *Radio Science*, **34**, 1025, 1999).

Rosenkranz, P. W., and C. D. Barnet, 2006: "Microwave radiative transfer model validation", *J. Geophys. Res*., **111**, D09S07, doi:10.1029/2005JD006008.

Rosenkranz, P. W., 2003: "Rapid radiative transfer model for AMSU/HSB channels", *IEEE Trans. Geosci. Rem. Sens.*, **41**, 362-368.

Rosenkranz, P. W., 2006: "Cloud liquid-water profile retrieval algorithm and validation," *J. Geophys. Res*., **111**, D09S08, doi:10.1029/2005JD005832.

Schaerer, G. and T. T. Wilheit, 1979: A passive microwave technique for profiling of atmospheric water vapor. *Radio Science*, **14**, 371-375.

Schwartz, M. J., 1997: Observations and Modeling of Atmospheric Oxygen Millimeter-wave Transmittance, Ph.D. Thesis, Mass. Inst. Of Tech., Dept. of Physics, Cambridge, MA.

Tretyakov, M., V. V. Parshin, M. A. Koshelev, V. N. Shanin, S. E. Myasnikova, and A. F. Krupnov, 2003: "Studies of 183 GHz water line: broadening and shifting by air, N_2 and O_2 and integral intensity measurements", *J. Molec. Spectros*., **218**, 239-245.

Wilheit, T. T., 1990: An algorithm for retrieving water vapor profiles in clear and cloudy atmospheres from 183 GHz radiometric measurements: Simulation studies. *J. App. Meteor.,* **29**, 508-515.

Wilheit, T. T., and K. D. Hutchinson, 1997: Water vapour profile retrievals from the SSM/T-2 data constrained by infrared-based cloud parameters. *Int. J. Remote Sensing*, **18**, 3263-3277.